



Time-dependent one-dimensional simulation of atmospheric dielectric barrier discharge in $N_2/O_2/H_2O$ using COMSOL Multiphysics

F. Sohbatzadeh¹ · H. Soltani¹

Received: 22 January 2018 / Accepted: 15 April 2018 / Published online: 30 April 2018
© The Author(s) 2018

Abstract

The results of time-dependent one-dimensional modelling of a dielectric barrier discharge (DBD) in a nitrogen–oxygen–water vapor mixture at atmospheric pressure are presented. The voltage–current characteristics curves and the production of active species are studied. The discharge is driven by a sinusoidal alternating high voltage–power supply at 30 kV with frequency of 27 kHz. The electrodes and the dielectric are assumed to be copper and quartz, respectively. The current discharge consists of an electrical breakdown that occurs in each half-period. A detailed description of the electron attachment and detachment processes, surface charge accumulation, charged species recombination, conversion of negative and positive ions, ion production and losses, excitations and dissociations of molecules are taken into account. Time-dependent one-dimensional electron density, electric field, electric potential, electron temperature, densities of reactive oxygen species (ROS) and reactive nitrogen species (RNS) such as: O, O^- , O^+ , O_2^- , O_2^+ , O_3 , N, N_2^+ , N_{2s} and N_2^- are simulated versus time across the gas gap. The results of this work could be used in plasma-based pollutant degradation devices.

Keywords Atmospheric pressure plasma · Dielectric barrier discharge · DBD simulation

Introduction

Identifying and studying the plasma and active species characteristics have attracted much attention because of successful experimental studies on atmospheric pressure plasma applications such as processing technology, engineering [1], sterilization and surface treatment [2–6]. Many works have been devoted to simulation of the atmospheric pressure plasmas. For example, Gadkari et al. modeled a co-axial DBD plasma reactor in pure helium using a 2-D fluid model in COMSOL Multiphysics [7]. They investigated the influence of partial packing on the discharge characteristics of the dielectric barrier discharge in helium. Pan et al. used the fluid model to carry out numerically the evolution features of the atmospheric-pressure CF_4 plasma in a dielectric barrier discharge [8]. Abidat et al. studied a one-dimensional model of atmospheric pressure helium gas

dielectric barrier discharge using COMSOL Multiphysics software [9]. Golubovskii et al, investigated spatio-temporal characteristics of the homogeneous barrier discharge in helium, numerically. They studied the influence of the elementary processes on the discharge by rate constants using a one-dimensional fluid model [10]. Various types of configurations for the derivation of electrical discharge at different working pressures have been reported. Dielectric barrier discharge (DBD) is one of the most famous working setup for a surface non-thermal electrical discharge. To prevent fast transition from atmospheric pressure electrical discharge to arc mode, one or two electrodes are covered by dielectric layers, therefore, they are kept away from the discharge contact [6]. Different processes such as electron impact ionization, photoionization, ionization by excited atoms and so on lead to stability of an electrical discharge [11]. Atmospheric pressure DBD as a process to generate active species, ozone, free radicals have been used for biological and medical applications such as sterilization and decontamination of environmental pollutions [12, 13].

In this work, electrical characteristics of DBD in $N_2/O_2/H_2O$ (0.78/0.21/0.01) together with the plasma species

✉ F. Sohbatzadeh
f.sohbat@umz.ac.ir

¹ Department of Atomic and Molecular Physics, Faculty of Basic Sciences, University of Mazandaran, Babolsar, Iran

were investigated by COMSOL Multiphysics 5.2 package. We performed time-dependent one-dimensional simulation of the DBD using reaction rates up to 99 reactions including effective processes such as electron attachment and detachment, surface charge accumulation, charged species recombination, conservation of negative and positive ions, ion production and losses, excitations and dissociations of molecules. Time-dependent one-dimensional electric field, electron density and temperature, densities of reactive oxygen and nitrogen species such as: O , O^- , O^+ , O_2^- , O_2^+ , O_3 , N , N_2^+ , N_{2s} and N_2^- , were evaluated versus time across the gas gap. It is well-known that the initiated reactions by reactive oxygen species (ROS) and reactive nitrogen species (RNS) play the key role in plasma disinfection and surface processing. Therefore, the results of this work could be used in plasma-based pollutant degradation devices.

Simulation model

Geometry description

In this paper, atmospheric pressure DBD is simulated. The plasma is driven by a sinusoidal alternating high voltage–power supply at 30 kV with a frequency of 27 kHz. The initial value for the electron density assumed to be 10^{13} m^{-3} , the gas pressure $1.01 \times 10^5 \text{ Pa}$ and the gas temperature 300 K. The reduced electron mobility and corresponding energy were obtained by executing BOLSIG+ [14, 15]. The results were $4 \times 10^{24} [1/v.s.m]$ and 5 [eV], respectively. The mass fraction of the discharge gas was $N_2/O_2/H_2O$ (0.78/0.21/0.01). As shown in Fig. 1, the gas gap between the two copper electrodes is 0.2 mm. The radius of round electrodes is assumed to be 5 cm, thicknesses of the electrode and quartz glass were assumed to be 0.2 and 0.1 mm, respectively.

Equations for performing DBD simulations

In this section, we introduce the governing equations of fluid dynamics that were used in this simulation. Surface chemistry was used to take into account reactions of different species and rate of production and losses at the electrodes surfaces [16]. The electron density and the electron mean energy were calculated by solving the pair of the propulsion and propagation equations. Equations (1) and (2) show the electron continuity and flux equation, respectively.

$$\frac{\partial n_e}{\partial t} + \nabla \cdot \vec{I}_e = R_e - (\vec{u} \cdot \nabla)n_e \tag{1}$$

$$\vec{I}_e = -(\vec{\mu}_e \cdot \vec{E})n_e - \vec{D}_e \cdot \nabla n_e \tag{2}$$

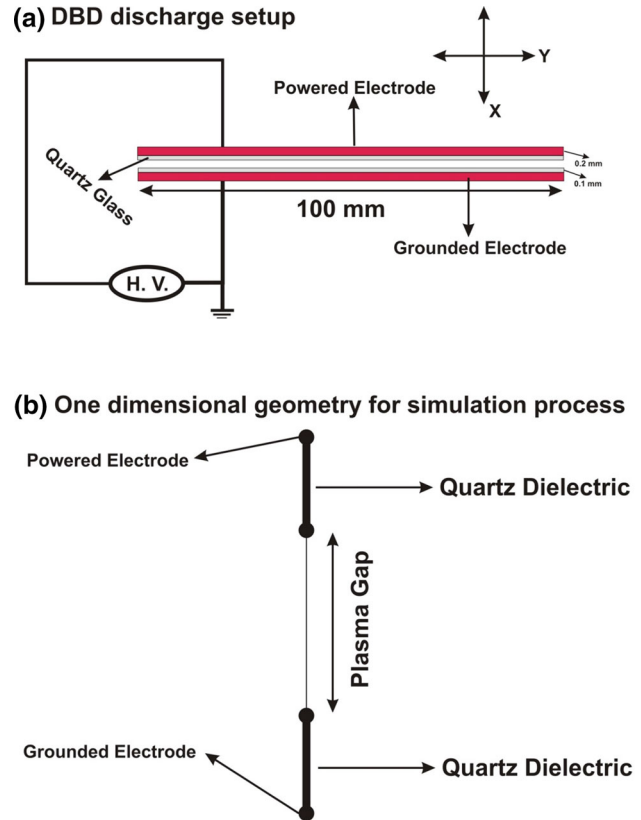


Fig. 1 a Setup of DBD. b One-dimensional geometry used in this simulation

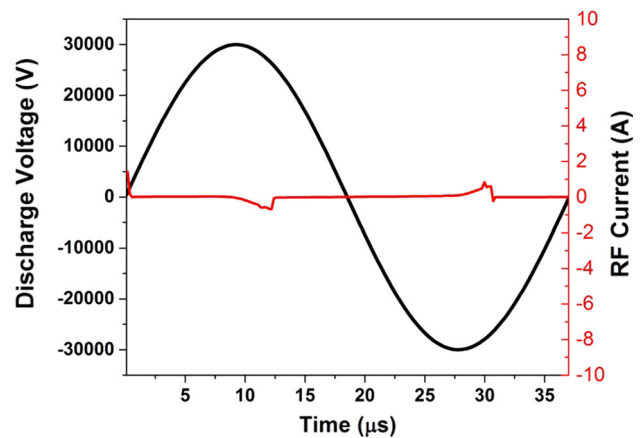


Fig. 2 Waveforms of the discharge voltage and the current (V–I) of the DBD

where n_e is the electron density, D_e electron diffusion coefficient, and \vec{I}_e is the electron flux, \vec{u} average fluid velocity of the species, R_e the rate of electron production.

The electron flux consists of two terms: a term caused by the electric field and the other by the density gradient. The electron energy density equation is:

$$\frac{\partial n_\epsilon}{\partial t} + \nabla \cdot \vec{I}_\epsilon + \vec{E} \cdot \vec{I}_\epsilon = R_\epsilon - (\vec{u} \cdot \nabla)n_\epsilon \tag{3}$$

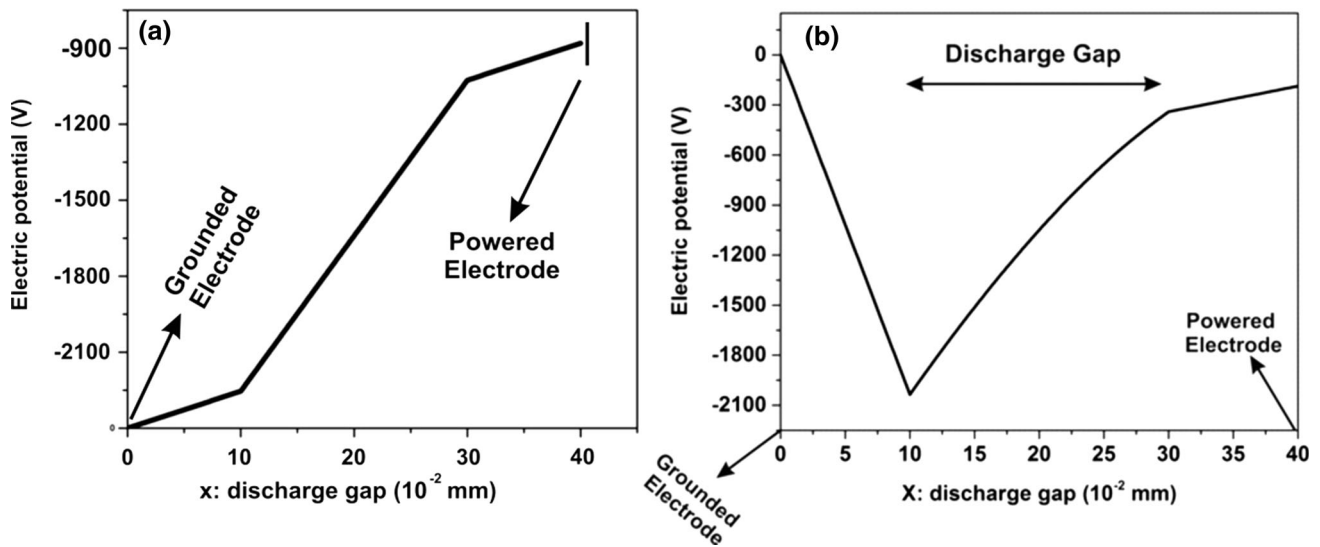


Fig. 3 Change of electric potential between the two electrodes a in the absence of plasma b in the presence of plasma

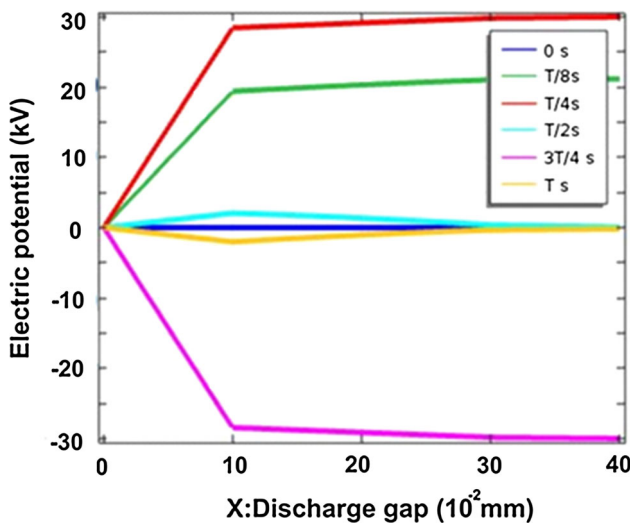


Fig. 4 Applied electric potential in different times versus discharge gap

$$\vec{\Gamma}_e = -(\vec{\mu}_e \cdot \vec{E}) \cdot n_e - \vec{D}_e \cdot \nabla n_e \tag{4}$$

where the term $\vec{E} \cdot \vec{\Gamma}_e$ indicates the amount of energy gained by the electron from the electric field. R_e the energy rate stemmed from inelastic collisions which is obtained from the following equation:

$$R_e = S_{en} + \frac{Q + Q_{gen}}{q} \tag{5}$$

S_{en} is the power dissipation, Q_{gen} is the main source of heat and q is the electron charge. D_e is the electron diffusion coefficient, μ_e is the energy mobility, and D_e is energy diffusion coefficient:

$$D_e = \mu_e T \quad D_e = \mu_e T_e \quad \mu_e = \frac{5}{3} \mu_e \tag{6}$$

We used the Townsend coefficients with the assumption that the electron source can be calculated from the following equation:

$$R_e = \sum_{j=1}^M x_j a_j N_n |\Gamma_e| \tag{7}$$

where M is the number of reactions, x_j the molar fraction of the target species for the reaction j , a_j the Townsend coefficient for the j th reaction and N_n the total number of neutral particles. Assuming that p is the number of non-elastic collisions of an electron, then we have:

$$R_e = \sum_{j=1}^P x_j a_j N_n |\Gamma_e| \Delta \epsilon_j \tag{8}$$

where $\Delta \epsilon_j$ is the energy dissipation from the j th reaction. In non-electron species, the following equations are solved for each mass fraction:

$$\rho \frac{\partial W_k}{\partial t} + \rho(\vec{u} \cdot \nabla) w_k = \nabla \cdot \vec{j}_k + R_k \tag{9}$$

where w_k is the density of ions, $\nabla \cdot \vec{j}_k$ the energy flux of the ions. The electrostatic field is calculated by the following equation:

$$\nabla \cdot (\epsilon_0 \epsilon_r E) = \rho \tag{10}$$

where ϵ_0 is the permittivity of vacuum, ϵ_r is the relative dielectric constant. According to the boundary conditions for electron flux and energy flux, we have the following relations:

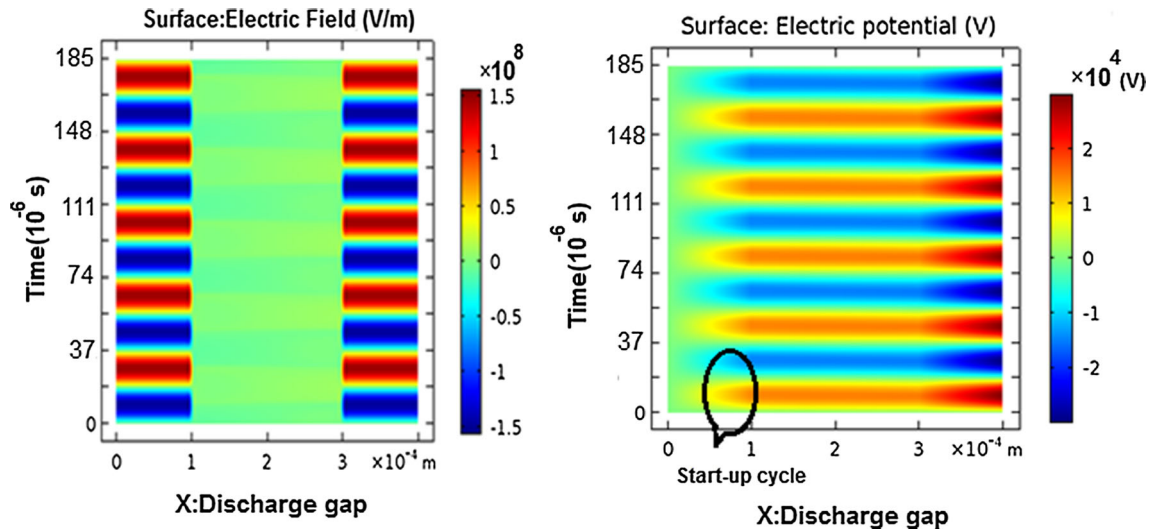


Fig. 5 Spatio-temporal evolutions of the electric field (left picture) and electric potential (right picture) versus the gap spacing

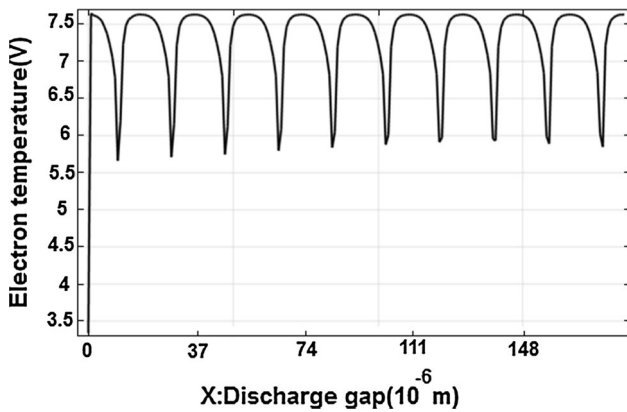


Fig. 6 Time evolution of the electron temperature at the center of the gap at $x = 2 \times 10^{-4}$ m

$$-\hat{n} \cdot \vec{\Gamma}_e = \left(\frac{1}{2} v_{eth} n_e \right) - \sum_p \gamma_p (\vec{\Gamma}_p \cdot \hat{n}) \tag{11}$$

$$-\hat{n} \cdot \vec{\Gamma}_e = \left(\frac{5}{6} v_{eth} n_e \right) - \sum_p \varepsilon_p \gamma_p (\vec{\Gamma}_p \cdot \hat{n}) \tag{12}$$

The second term on the right side of Eq. (11) indicates that the electron is produced according to the secondary emission and γ is the secondary emission coefficient. On the surface of the electrodes, ions and excited species become neutralized by surface reactions. Surface interactions on the electrodes are simulated using the coefficient β_j , which it determines the probability of operating j species. For the ion species in the discharge, the conjugation equation is as follows:

$$\frac{\partial n_i}{\partial t} + \nabla \cdot (n_i \vec{u}) = -\nabla \cdot (\mu_i n_i q_i \nabla \varphi - D_i \nabla n_i) + S_i \tag{13}$$

φ and S_i show the electrostatic potential and rate of change of electron density, respectively.

Simulation results

The evolutions of active species density, electron temperature and electric potential in the DBD gap are investigated in this work. Figure 2 shows the $V-I$ characteristics of the electrical discharge across the gap in one period. In this figure, the change in current depicts breakdown of the gas gap. That is, in each cycle, there are two breakdown events.

As shown in Fig. 3, due to aggregation of positive charges on dielectric covering the grounded electrode, electric potential between two electrodes is changed.

The evolutions of the applied voltage across the gap are indicated in Fig. 4 in different times.

The spatio-temporal evolutions of the electric field and potential between the two electrodes are indicated in Fig. 5. As shown in this figure, in the presence of electrical discharge, electric field in the gap is reduced because of the plasma diamagnetic property.

Time evolutions of the electron temperature are appeared in Fig. 6 for center of the gap. It is seen that the electron temperature changes twice in each period due to the two discharge events in a cycle as indicated in Fig. 2. Spatio-temporal evolutions of the electron density are depicted in Fig. 7 versus the gap spacing. It is seen that the discharge occurs twice in each cycle, one in the positive and the other in the negative half cycle of the voltage. The

Fig. 7 Spatio-temporal evolutions of the electron density versus the gap spacing

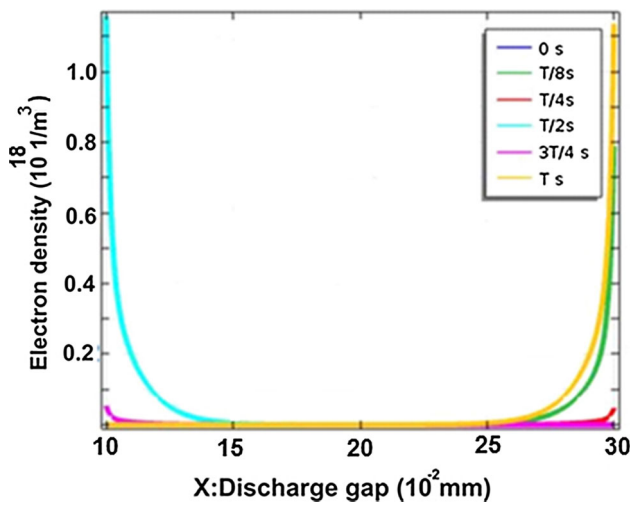
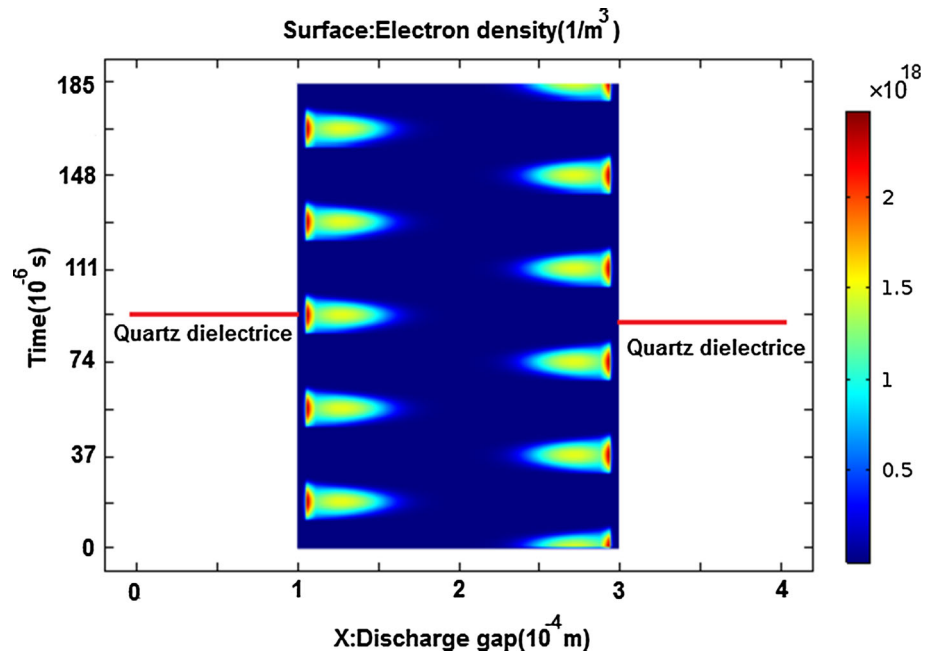


Fig. 8 Electron density in discharge gap in different times

first discharge event initiates near the powered electrode corresponds to the right hand side of the picture. The maximum electron density is about $1.2 \times 10^{18} \text{ m}^{-3}$. It is seen that the electric field and the potential changes periodically versus position. The root mean square of the electric field can be used to investigate the sheath region [17, 18].

The evolutions for the electron density and temperature distribution across the gap in different times are shown in Figs. 8 and 9, respectively.

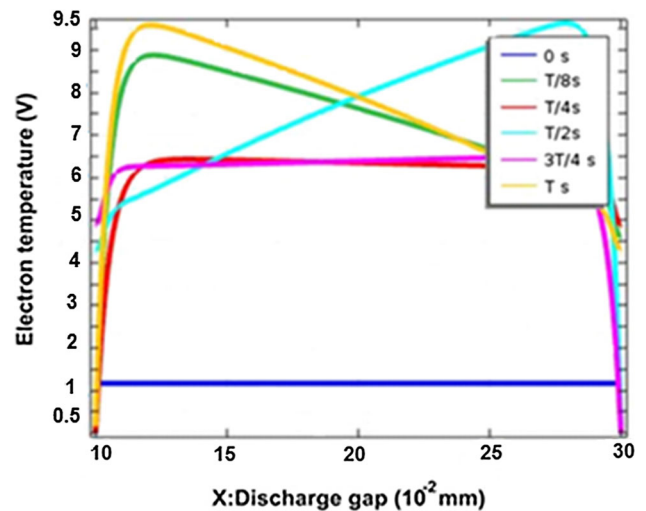


Fig. 9 Distribution of electron temperature across the discharge gap at the Time of T

Figure 10 shows the two-dimensional simulation image of the electron temperature between the two electrodes. The electron temperature grows and diminishes corresponding to each discharge event.

Variations of N_2^+ and N_2s (excited nitrogen) densities are indicated in Figs. 11.

Figure 12 shows the distribution of atomic nitrogen and oxygen at the time of T . For positive and negative oxygen molecule, variations of O_2^- and O_2^+ are depicted in

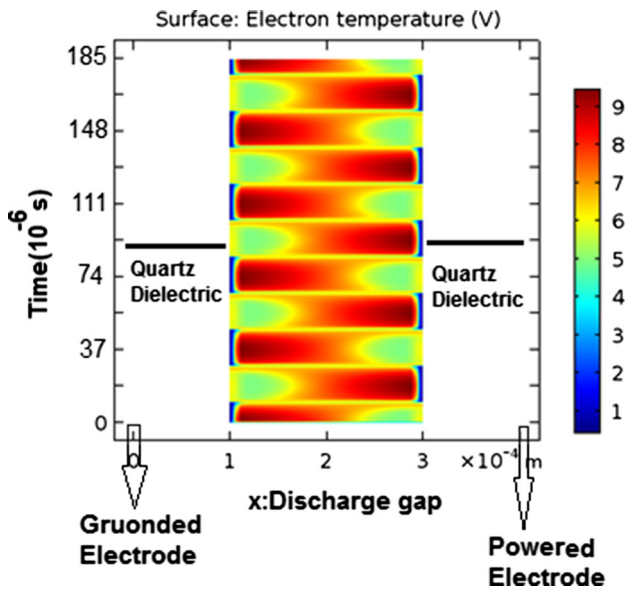


Fig. 10 Spatio-temporal electron temperature evolutions in discharge gap

Fig. 13. Distributions of ionized and atomic oxygen, O^+ and O^- are depicted in figure Fig. 14.

The reactions due to electron impact inside the gas gap are given in Tables 1 and 2. The reactions of electron impact with active species of nitrogen including: metastable nitrogen N_{2s} , nitrogen molecule N_2 and singly ionized nitrogen molecule N_2^+ are depicted in Table 1 [14, 19]. The reactions of electron impact with oxygen and water vapor molecules are shown in Table 2. In Table 2, the reaction rates R_1 till R_{14} are for oxygen molecules while the rates R_{15} till R_{22} are for the water vapor molecules [14, 19]. Two and three body reaction rates among the atoms and molecules are depicted in Table 3. The surface reactions are also given in Table 4.

Spatio-temporal simulation results of N_{2s} , N_2^- and N_2^+ densities across the discharge gap are shown in Figs. 15, 16 and 17, respectively. The variation of ozone concentration as an important radical species in process of sterilization and pollution decontamination is shown in Fig. 18. It is seen that the ozone concentration increases versus time. The accumulation of the ozone inside the discharge gap is due to its long enough life time. The discharge event duration in the DBD is in the order of micro-seconds, while the ozone life time is in the order of several minutes [20].

Conclusions

Atmospheric DBD discharge has drawn great interest as a device for sterilization and decontamination of pollutions. To identify and study the DBD characteristics and active species densities, we performed a simulation work by COMSOL Multiphysics package. To realize the density evolutions more precise we took into account 99 rate equations. The rates include elastic scattering of the electrons by the gas mixture molecules, electron impact excitation and ionization of the nitrogen, oxygen and water vapor molecules, two and three body collisions among the atoms, molecules and ions. It was revealed by examining the densities of the produced ROS and RNS that they are responsible for plasma disinfection and surface treatment processing based on their substantial number densities. Electron density and temperature evolutions were examined across the gap versus time. Spatio-temporal evolutions of the electric field and potential showed significant changes inside the discharge gap due to presence of the charged plasma species. One of the important results was the growing density of the ozone. It is produced in each discharge event and accumulated inside the gap. Its density

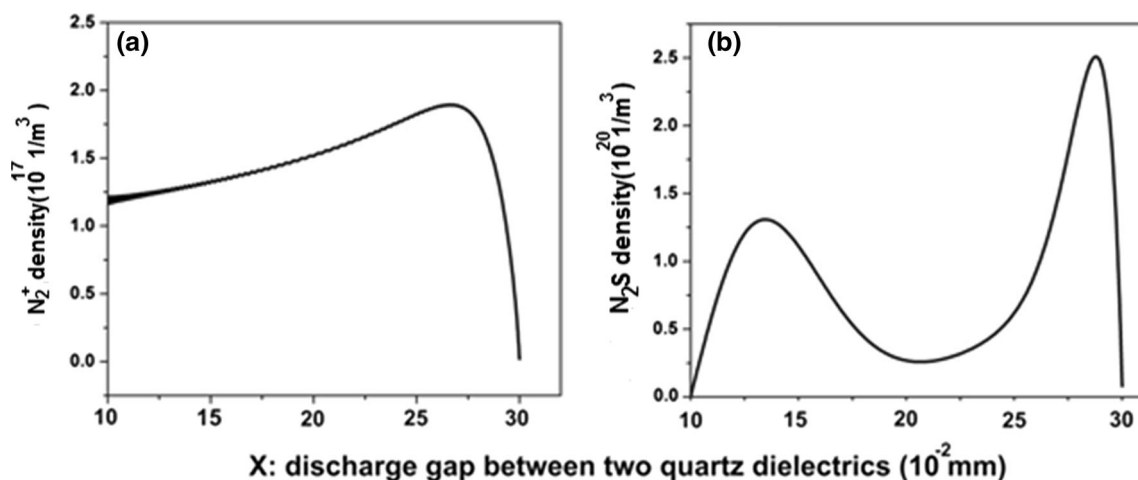


Fig. 11 Density distribution of a) N_2^+ and b) N_{2s} in the DBD gap at the time of T



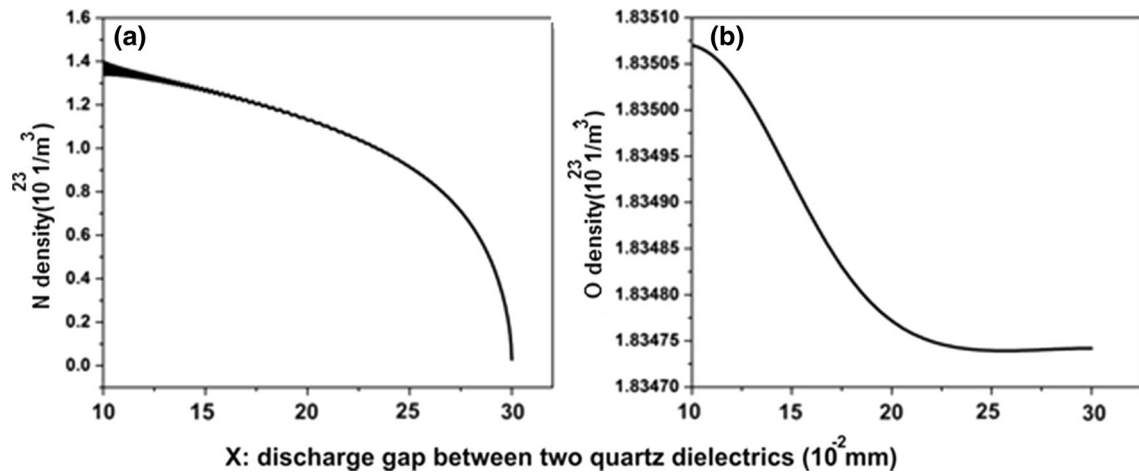


Fig. 12 Density distribution of a N and b O in the DBD gap at the time of T

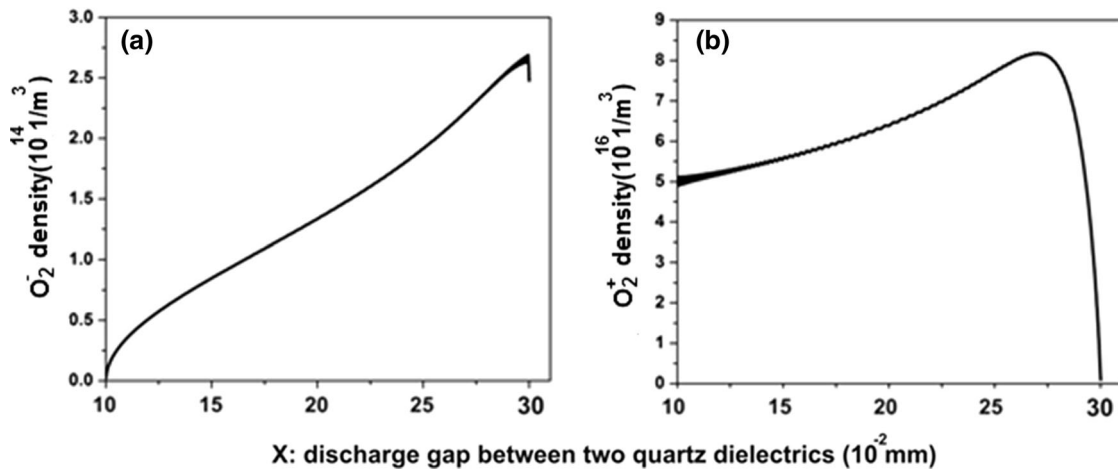


Fig. 13 Density distribution of a O_2^- and b O_2^+ in the DBD gap at the time of T

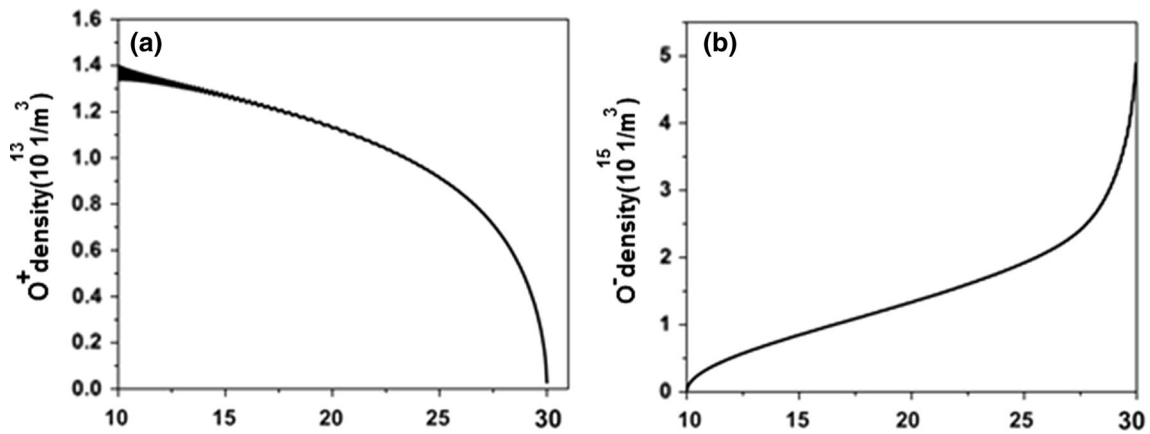


Fig. 14 a Variations of O^+ and b O^- across the discharge gap for $t = T$

Table 1 The reactions of electron impact with active species of nitrogen (metastable nitrogen N_{2s} , Nitrogen molecule N_2 , singly ionized nitrogen molecule N_2^+) [14, 19]

Reaction	Formula	Type	ΔE (ev)
R ₁	$e + N_2 \rightarrow e + N_2$	Elastic scattering	$m/M = 0.0000195$
R ₂	$e + N_2 \rightarrow e + N_{2s}$	Excitation	0.2889
R ₃	$e + N_2 \rightarrow e + N_{2s}$	Excitation	0.5742
R ₄	$e + N_2 \rightarrow e + N_{2s}$	Excitation	0.8559
R ₅	$e + N_2 \rightarrow e + N_{2s}$	Excitation	1.1342
R ₆	$e + N_2 \rightarrow e + N_{2s}$	Excitation	1.4088
R ₇	$e + N_2 \rightarrow e + N_{2s}$	Excitation	1.6801
R ₈	$e + N_2 \rightarrow e + N_{2s}$	Excitation	1.9475
R ₉	$e + N_2 \rightarrow e + N_{2s}$	Excitation	2.2115
R ₁₀	$e + N_2 \rightarrow e + N_{2s}$	Excitation	2.4718
R ₁₁	$e + N_2 \rightarrow e + N_{2s}$	Excitation	2.7284
R ₁₂	$e + N_2 \rightarrow e + N_{2s}$	Excitation	2.9815
R ₁₃	$e + N_2 \rightarrow e + N_{2s}$	Excitation	3.231
R ₁₄	$e + N_2 \rightarrow e + N_{2s}$	Excitation	3.4769
R ₁₅	$e + N_2 \rightarrow e + N_{2s}$	Excitation	3.7191
R ₁₆	$e + N_2 \rightarrow e + N_{2s}$	Excitation	3.9576
R ₁₇	$e + N_2 \rightarrow e + N_{2s}$	Excitation	6.725
R ₁₈	$e + N_2 \rightarrow e + N_{2s}$	Excitation	8.05
R ₁₉	$e + N_2 \rightarrow e + N_{2s}$	Excitation	8.217
R ₂₀	$e + N_2 \rightarrow e + N_{2s}$	Excitation	8.95
R ₂₁	$e + N_2 \rightarrow e + N_{2s}$	Excitation	8.974
R ₂₂	$e + N_2 \rightarrow e + N_{2s}$	Excitation	9.562
R ₂₃	$e + N_2 \rightarrow e + N_{2s}$	Excitation	9.665
R ₂₄	$e + N_2 \rightarrow e + N_{2s}$	Excitation	10.174
R ₂₅	$e + N_2 \rightarrow 2e + N_2^+$	Ionization	15.581

Table 2 The reactions of electron impact with oxygen and water vapor molecules [14, 19]

Reaction	Formula	Type	ΔE (ev)
R ₁	$e + O_2 \rightarrow e + O_2$	Elastic scattering	$m/M = 0.000017$
R ₂	$e + O_2 \rightarrow O + O^-$	Attachment	0
R ₃	$e + O_2 \rightarrow e + O_2$	Excitation	0.02
R ₄	$e + O_2 \rightarrow e + O_2$	Excitation	0.193
R ₅	$e + O_2 \rightarrow e + O_2$	Excitation	0.386
R ₆	$e + O_2 \rightarrow e + O_2$	Excitation	0.579
R ₇	$e + O_2 \rightarrow e + O_2$	Excitation	0.772
R ₈	$e + O_2 \rightarrow e + O_2$	Excitation	0.977
R ₉	$e + O_2 \rightarrow e + O_2$	Excitation	1.627
R ₁₀	$e + O_2 \rightarrow e + O_2$	Excitation	4.5
R ₁₁	$e + O_2 \rightarrow e + O_2$	Excitation	6.1
R ₁₂	$e + O_2 \rightarrow e + O_2$	Excitation	8.4
R ₁₃	$e + O_2 \rightarrow e + O_2$	Excitation	9.3
R ₁₄	$e + O_2 \rightarrow 2e + O_2^+$	Ionization	12.072
R ₁₅	$e + H_2O \rightarrow e + H_2O$	Elastic scattering	$m/M = 0.00003043$
R ₁₆	$e + H_2O \rightarrow H_2O^-$	Attachment	0
R ₁₇	$e + H_2O \rightarrow e + H_2O$	Excitation	0.206
R ₁₈	$e + H_2O \rightarrow e + H_2O$	Excitation	0.459
R ₁₉	$e + H_2O \rightarrow e + H_2O$	Excitation	1.058
R ₂₀	$e + H_2O \rightarrow e + H_2O$	Excitation	8.445
R ₂₁	$e + H_2O \rightarrow e + H_2O$	Excitation	14.052
R ₂₂	$e + H_2O \rightarrow e + e + H_2O^+$	Ionization	13.76



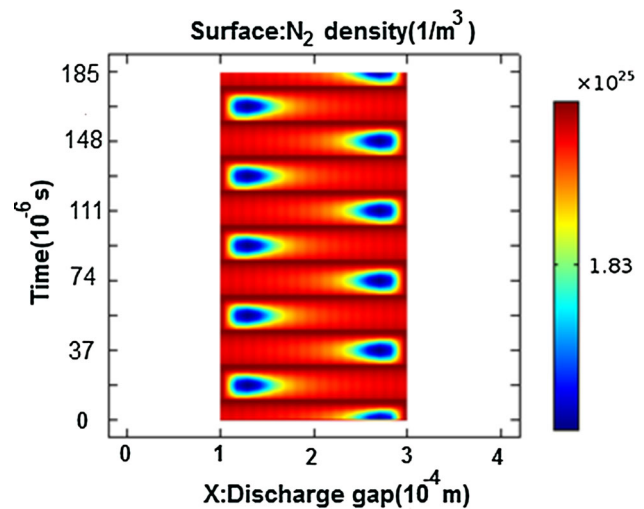
Table 3 Two and three body reactions between the atoms and molecules, the unit of the two and three body rates are m^3/s and m^6/s , respectively [19]

Reaction	Formula	Rate (m^3 or m^6/s mol)
R ₁	$\text{O} + \text{O}_2 + \text{O}_2 \rightarrow \text{O}_3 + \text{O}_2$	6×10^{-46}
R ₂	$\text{O} + \text{O}_2 + \text{N}_2 \rightarrow \text{O}_3 + \text{N}_2$	5.6×10^{-46}
R ₃	$\text{O} + \text{O}_3 \rightarrow \text{O}_2 + \text{O}_2$	8×10^{-18}
R ₄	$\text{O} + \text{NO}_2 \rightarrow \text{NO} + \text{O}_2$	5.6×10^{-7}
R ₅	$\text{O} + \text{NO}_3 \rightarrow \text{O}_2 + \text{NO}_2$	1.7×10^{-17}
R ₆	$\text{O} + \text{N}_2\text{O}_5 \rightarrow \text{NO}_2 + \text{NO}_2 + \text{O}_2$	1×10^{-22}
R ₇	$\text{N} + \text{O}_2 \rightarrow \text{NO} + \text{O}$	1.5×10^{-7}
R ₈	$\text{N} + \text{O}_3 \rightarrow \text{N} + \text{O}_2$	10×10^{-22}
R ₉	$\text{N} + \text{NO} \rightarrow \text{N}_2 + \text{O}$	2.1×10^{-11}
R ₁₀	$\text{NO} + \text{O}_3 \rightarrow \text{NO}_2 + \text{O}_2$	3×10^{-18}
R ₁₁	$\text{N} + \text{NO}_2 \rightarrow \text{N}_2\text{O} + \text{O}$	5.8×10^{-18}
R ₁₂	$\text{NO}_2 + \text{O}_3 \rightarrow \text{NO}_3 + \text{O}_2$	1.4×10^{-19}
R ₁₃	$\text{O}_2 + \text{O}_2 \rightarrow \text{O}_3 + \text{O}$	2.95×10^{-27}
R ₁₄	$\text{N}_2 + \text{O}_2 \rightarrow \text{N}_2\text{O} + \text{O}$	6×10^{-20}
R ₁₅	$\text{O}^- + \text{O} \rightarrow \text{O}_2 + \text{e}$	2×10^{-16}
R ₁₆	$\text{O}^- + \text{O}_2 \rightarrow \text{O}_3 + \text{e}$	3×10^{-16}
R ₁₇	$\text{O}^- + \text{O}_2 \rightarrow \text{O} + \text{O}_2 + \text{e}$	6.9×10^{-16}
R ₁₈	$\text{O}_2^- + \text{O} \rightarrow \text{O}^- + \text{O}_2$	1.5×10^{-16}
R ₁₉	$\text{O}^- + \text{O}_3 \rightarrow \text{O}_2 + \text{O}_2 + \text{e}$	1.02×10^{-17}
R ₂₀	$\text{O}^- + \text{O}_3 \rightarrow \text{O}_2^- + \text{O}_2$	3.01×10^{-16}
R ₂₁	$\text{O}_2^- + \text{O} \rightarrow \text{O}_3 + \text{e}$	1.5×10^{-16}
R ₂₂	$\text{O} + \text{O}_3 \rightarrow \text{O}_2 + \text{O} + \text{O}$	1.2×10^{-16}
R ₂₃	$\text{O} + \text{O}_2 \rightarrow \text{O}_3 + \text{O}_2$	6×10^{-16}
R ₂₄	$\text{O}_2 \rightarrow \text{O}_2$	1×10^{-5}
R ₂₅	$\text{e} + \text{H}_2\text{O} \rightarrow \text{H} + \text{OH} + \text{e}$	2.6×10^{-18}
R ₂₆	$\text{O} + \text{H}_2\text{O} \rightarrow 2\text{OH}$	2.3×10^{-16}
R ₂₇	$\text{OH} + \text{H} \rightarrow \text{H}_2 + \text{O}$	1.38×10^{-20}
R ₂₈	$\text{O} + \text{OH} \rightarrow \text{O}_2 + \text{H}$	2.3×10^{-17}
R ₂₉	$\text{H} + \text{O}_2 \rightarrow \text{H}_2\text{O}$	4.8×10^{-39}
R ₃₀	$\text{OH} + \text{H} \rightarrow \text{H}_2\text{O}$	8.6×10^{-37}
R ₃₁	$\text{OH} + \text{O} \rightarrow \text{H} + \text{O}_2$	3.8×10^{-17}
R ₃₂	$\text{N} + \text{OH} \rightarrow \text{NO} + \text{H}$	3.8×10^{-17}
R ₃₃	$\text{NO} + \text{H}_2\text{O} \rightarrow \text{HNO}_3$	5.6×10^{-39}
R ₃₄	$\text{NO} + \text{H}_2\text{O} \rightarrow \text{HNO} + \text{O}_2$	9.1×10^{-25}
R ₃₅	$\text{NO} + \text{H}_2\text{O} \rightarrow \text{NO}_2 + \text{OH}$	3.7×10^{-18}
R ₃₆	$\text{NO} + \text{NO}_3 \rightarrow \text{NO}_2 + \text{NO}_2$	1.6×10^{-17}
R ₃₇	$\text{N}_2\text{O}_5 + \text{H}_2\text{O} \rightarrow \text{HNO}_3 + \text{HNO}_3$	5×10^{-27}
R ₃₈	$\text{HNO} + \text{O}_2 \rightarrow \text{NO} + \text{H}_2\text{O}$	5.25×10^{-18}

reaches to 10^{14} m^{-3} in our simulations. On the other hand, the electron density and the maximum electron temperature are proved to be about 10^{18} m^{-3} and 9.5 eV, respectively.

Table 4 Surface reactions [19]

Reaction	Formula	Sticking coefficient
R ₁	$\text{N}_{2s} \rightarrow \text{N}_2$	1
R ₂	$\text{N}_2^+ \rightarrow \text{N}_2$	1
R ₃	$\text{O}_2\text{a1d} \rightarrow \text{O}_2$	1
R ₄	$\text{O}_2\text{45} \rightarrow \text{O}_2$	1
R ₅	$\text{O}_2\text{b1s} \rightarrow \text{O}_2$	1
R ₆	$\text{O}_2 \rightarrow \text{O}_2$	1
R ₇	$\text{O}_2^+ \rightarrow \text{O}_2$	1
R ₈	$\text{O}^+ \rightarrow \text{O}$	1
R ₉	$\text{O}^- \rightarrow \text{O}$	1
R ₁₀	$\text{O1s} \rightarrow \text{O}$	1
R ₁₁	$\text{O1d} \rightarrow \text{O}$	1
R ₁₂	$\text{N}^+ \rightarrow \text{N}$	1
R ₁₃	$\text{N}_{2s} \rightarrow \text{N}_2$	1
R ₁₄	$\text{N}_2^+ \rightarrow \text{N}_2$	1

**Fig. 15** Spatio-temporal evolutions of N_2 density at discharge gap between the two quartz dielectrics

Among the ROS (O , O^- , O^+ , O_2^- , O_2^+ and O_3), O_2^+ and O^- have considerable densities and that for RNS (N , N_2^+ , N_{2s} and N_2^-) N and N_{2s} have the highest densities. The initiated reactions by ROS and RNS ozone, atomic oxygen and excited state of oxygen molecules play the key role in plasma disinfection and surface processing. Therefore, the results of this work could be used in plasma-based pollutant degradation devices.

Open Access This article is distributed under the terms of the Creative Commons Attribution 4.0 International License (<http://creativecommons.org/licenses/by/4.0/>)



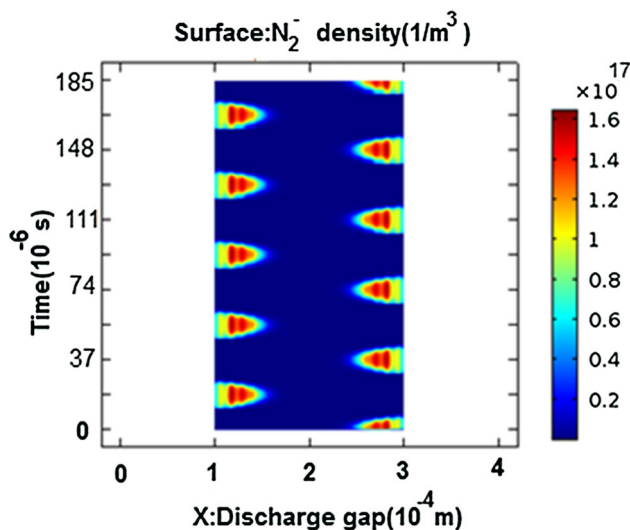


Fig. 16 Spatio-temporal evolutions of N_2^- density in the discharge gap

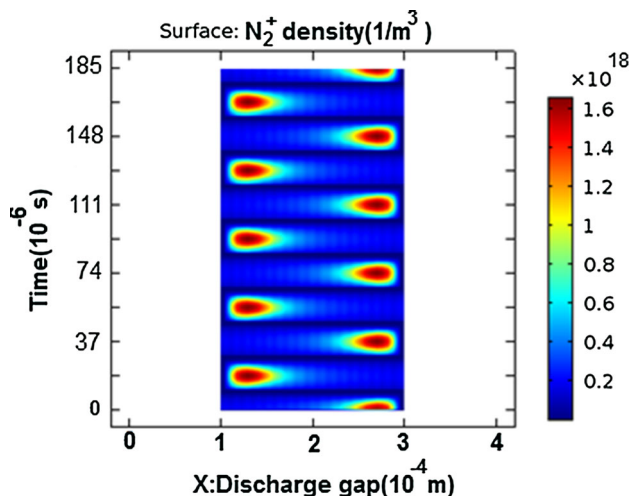


Fig. 17 Spatio-temporal evolutions of N_2^+ density in the discharge gap

creativecommons.org/licenses/by/4.0/), which permits unrestricted use, distribution, and reproduction in any medium, provided you give appropriate credit to the original author(s) and the source, provide a link to the Creative Commons license, and indicate if changes were made.

References

- Keidar, M., Beilis, I.: Plasma Engineering: Applications from Aerospace to Bio and Nanotechnology. Academic Press, Oxford (2013)
- Sohbatzadeh, F., Colagar, A.H., Mirzanejhad, S., Mahmodi, S.: *E. coli*, *P. aeruginosa*, and *B. cereus* bacteria sterilization using afterglow of non-thermal plasma at atmospheric pressure. Appl. Biochem. Biotechnol. **160**, 1978–1984 (2010)
- Sohbatzadeh, F., Mirzanejhad, S., Ghasemi, M., Talebzadeh, M.: Characterization of a non-thermal plasma torch in streamer mode

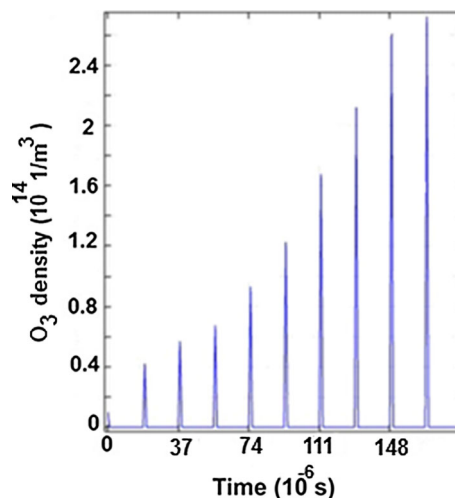


Fig. 18 Production and accumulation of ozone in the DBD reactor versus time

- and its effect on polyvinyl chloride and silicone rubber surfaces. J. Electrostat. **71**, 875–881 (2013)
- Fridman, A.: Plasma Chemistry. Cambridge University Press, Cambridge (2008)
 - Fridman, G., Gutsol, A., Shekhter, A.B., Vasilets, V.N., Fridman, A.: Plasma Processes Polym. **5**(6), 503–533 (2008)
 - Roth, J.R.: Industrial Plasma Engineering: Volume 2-Applications to Nonthermal Plasma Processing. CRC Press, Boca Raton (2001)
 - Gadkari, S., Tu, X., Gu, S.: Fluid model for a partially packed dielectric barrier discharge plasma reactor. Phys. Plasmas **24**, 093510 (2017)
 - Pan, J., Li, L., Chen, B., Song, Y., Zhao, Y., Xiu, X.: Numerical simulation of evolution features of the atmospheric-pressure CF₄ plasma generated by the pulsed dielectric barrier discharge. Eur. Phys. J. D **70**, 136 (2016)
 - Abidat, R., Rebiai, S., Benterrouche, L.: Numerical simulation of atmospheric dielectric barrier discharge in helium gas using COMSOL Multiphysics. In: Systems and Control (ICSC), 2013 3rd International Conference on (pp. 134–139). IEEE (2013)
 - Golubovskii, Y.B., Maiorov, V.A., Behnke, J., Behnke, J.F.: Modelling of the homogeneous barrier discharge in helium at atmospheric pressure. J. Phys. D **36**, 39 (2002)
 - Raizer, Y.P.: Gas Discharge Physics, Springer, Berlin (1997)
 - Tanaka, Y., Yasuda, H., Kurita, H., Takashima, K., Mizuno, A.: Analysis of the inactivation mechanism of bacteriophage ϕ X174 by atmospheric pressure discharge plasma. IEEE Trans. Ind. Appl. **50**, 1397–1401 (2014)
 - Kirkpatrick, M., Dodet, B., Odic, E.: Atmospheric pressure humid argon DBD plasma for the application of sterilization-measurement and simulation of hydrogen, oxygen, and hydrogen peroxide formation. Int. J. Plasma Env. Sci. Technol. **1**, 96–101 (2007)
 - BOLSIG+ , Electron Boltzmann equation solver. <https://www.bolsig.laplace.univ-tlse.fr>. Accessed 1 Nov 2017
 - Bolz, R.E., Tuve, G.L. Handbook of Tables for Applied Engineering Science, pp. 168–169. Chemical Rubber Co, Cleveland, Ohio (1970)
 - Lieberman, M.A., Lichtenberg, A.J.: Principles of Plasma Discharges and Materials Processing. John Wiley, Hoboken (2005)
 - Balcon, N., Hagelaar, G.J.M., Boeuf, J.P.: Numerical model of an argon atmospheric pressure RF discharge. IEEE Trans. Plasma Sci. **36**(5), 2782–2787 (2008)

18. Chirokov, A., Khot, S.N., Gangoli, S.P., Fridman, A., Henderson, P., Gutsol, A.F., Dolgopolsky, A.: Numerical and experimental investigation of the stability of radio-frequency (RF) discharges at atmospheric pressure. *Plasma Sour. Sci. Technol.* **18**(2), 025025 (2009)
19. LXCAT, electron scattering database, University of Toulouse, France. www.lxcat.net. Accessed 1 Nov 2017
20. McClurkin, J.D., Maier, D.E., Ileleji, K.E.: Half-life time of ozone as a function of air movement and conditions in a sealed container. *J. Stored Prod. Res.* **55**, 41–47 (2013)

Publisher's Note

Springer Nature remains neutral with regard to jurisdictional claims in published maps and institutional affiliations.

